

# Impact of Charge on Strange Compact Stars in Rastall Theory

Malick Sallah <sup>1,2</sup>  and Muhammad Sharif <sup>1,\*</sup> 

<sup>1</sup> Department of Mathematics and Statistics, The University of Lahore, 1-KM Defence Road, Lahore 54000, Pakistan; malick.sallah@utg.edu.gm

<sup>2</sup> Department of Mathematics, The University of the Gambia, Serrekunda P.O. Box 3530, The Gambia

\* Correspondence: msharif.math@pu.edu.pk

**Abstract:** Within the framework of Rastall theory, we investigate the impact of charge on the structural development of different types of spherically symmetric anisotropic stars. To do so, we present modified field equations based upon the Finch–Skea metric potentials expressed in terms of three parameters ( $A, B, C$ ). These constants are determined using suitable matching conditions and observational data for compact objects which include Her X-1, SAX J 1808.4-3658, PSR J038-0842, LMC X-4 and SMC X-1. The equation of state offered by the MITT bag model for quark–gluon plasma is used to investigate the inner structure and other characteristics of these compact objects. For a fixed bag constant,  $B = 60 \text{ MeV}/\text{fm}^3$ , and two sets of the Rastall and charge parameters,  $\zeta = 0.255, 0.259$  and  $\tilde{Q} = 0.2, 0.7$ , respectively, we analyze the consistency of the matter variables in the model and other physical parameters such as energy conditions, stellar mass, compactness, and surface redshift. In addition, we assess the stability of the constructed model through two different approaches. It is found that the obtained model is physically viable and stable.

**Keywords:** MITT bag model; Rastall theory; quark stars

**PACS:** 04.40.Dg; 04.40.-b; 04.50.Kd



Academic Editor: Fridolin Weber,  
Jose Carlos Neves De Araujo,  
Hemily Gomes Marciano Fortes  
and Emmanuel N. Saridakis

Received: 24 October 2024

Revised: 13 January 2025

Accepted: 14 January 2025

Published: 16 January 2025

**Citation:** Sallah, M.; Sharif, M.  
Impact of Charge on Strange Compact  
Stars in Rastall Theory. *Universe* **2025**,  
*11*, 25. [https://doi.org/10.3390/  
universe11010025](https://doi.org/10.3390/universe11010025)

**Copyright:** © 2025 by the authors.  
Licensee MDPI, Basel, Switzerland.  
This article is an open access article  
distributed under the terms and  
conditions of the Creative Commons  
Attribution (CC BY) license  
([https://creativecommons.org/  
licenses/by/4.0/](https://creativecommons.org/licenses/by/4.0/)).

## 1. Introduction

While general relativity (GR) has been extensively tested in weak gravitational fields, its predictions in strong-field regimes, such as near black holes, remain an active area of investigation and experimental verification [1,2]. Moreover, GR does not easily explain the quicker speed at which the universe is claimed to expand with time, without postulating the existence of dark matter and dark energy. Such problems, among many other factors, call for alterations to the GR. There are two principal approaches to the modification of GR. The first of these seeks to keep GR in its simplest form by adding extra terms to the Lagrangian density that in turn changes the field equations, while the second approach seeks to alter some of the basic principles of GR. The Rastall theory of gravitation belongs to the second category. In this case, the configuration of the covariant divergence of the stress–energy tensor is proportional to the divergence of the curvature scalar,  $\mathcal{R}$  [3,4]. This implies that one has to give up the classical notion of conservation of energy. Hence, the Rastall theory exhibits a matter and geometry interaction that is not minimal in curved spacetimes. Nevertheless, in flat spacetimes devoid of curvature, the energy–momentum tensor obeys a conservation principle leading to the field equations being equivalent to vacuum Einstein field equations.

Rastall gravity has been under scrutiny, particularly in relation to the criticism on the non-conservation of the energy–momentum tensor [5,6]. Nonetheless, this so-called

defect can be interpreted as an effect resulting from the curvature of spacetime or even net energy production in specific systems. The discourse surrounding Rastall gravity is indeed complex and multifaceted. We acknowledge the contrasting views presented by Visser [5] and Golovnev [6], who argue that Rastall gravity is effectively a redefinition of the energy–momentum tensor in GR. These arguments were accordingly countered by Darabi et al. [7], who maintained that Rastall theory introduces a non-minimal coupling that distinguishes it from GR. Visser claimed that from the Rastall energy–momentum tensor  $\tilde{T}_{\psi\chi}$ , one can always reconstruct the physical quantity  $T_{\psi\chi}$ , and vice versa. We, however, do not agree with his point because if this is the motivation for proving Rastall theory to be equivalent to GR, then one can easily do this for other matter geometry coupled theories, in particular,  $f(\mathcal{R}, T)$  gravity, which was proposed through modifying the Einstein–Hilbert action. It is thus not a valid point to say that GR and Rastall theory are equivalent to each other.

Another point often raised against the theory is its lack of a Lagrangian formulation, despite the fact that in cosmology and astrophysics, it has given good results. Attempts to construct a proper Lagrangian, as of now, have not been successful, thus creating uncertainty regarding its viability. Notwithstanding these hindrances, the merits of Rastall theory are clearly pronounced, as many theoretical and observational works have come up in recent times [8–15]. The lack of a Lagrangian does not compromise the robustness of our results within the current framework. The field equations used in this study are well defined, and the solutions we derive are consistent with physical conditions such as energy conservation, stability, and regularity at the stellar center. Moreover, by explicitly examining how Rastall gravity modifies the structure of compact stars compared to GR, we demonstrate that the theory retains significant predictive power despite its theoretical limitations.

We emphasize that many successful theories, including GR during its early development, initially lacked a fully developed Lagrangian formulation but were later refined as theoretical tools evolved. Similarly, our findings should be viewed as part of a broader effort to explore the utility of Rastall gravity in astrophysical contexts, while recognizing the need for further theoretical advancements. By providing physically viable and stable models of compact stars, this work demonstrates the practical relevance of Rastall gravity even within its current formulation, underscoring its potential as a stepping stone toward more comprehensive theories. Additionally, the concept of modified gravitational theories that do not hold the energy conservation is not a novel one since different variations of the non-conservative models have been suggested over the years. One of the first examples of such a model is the Einstein trace-free theory, referred to as unimodular gravity [16]. It is interesting to observe that even though unimodular gravity,  $f(\mathcal{R}, T)$  gravity, Rastall theory, and GR stand out in their individual uses, they are geometrically equivalent. This arises because they share the same pressure isotropy equations, which govern the behavior of their gravitational potentials [7,17–19].

Stars play an enormous role in not only the formation but also in the growth and evolutionary processes of existing cosmic structures across the universe. The evolving and three-dimensional structures of galactic objects has been the focus of many astrophysicists for years. The stellar material possesses an inward force due to its mass. This is counter-balanced by an outward force due to the nuclear processes occurring within the matter. Nevertheless, there exists a limit at which this force ceases to act against gravitational pull and the star experiences collapse under its own weight leading to their annihilation and the formation of compact objects. Due to their unique structure and interesting shapes, a lot of astrophysicists and researchers are fascinated with neutron stars. These types of stars are in hydrostatic equilibrium due to the opposing forces of gravity and neutron degeneracy pressure. A quark star is a hypothetical dense state of matter that may exist between a neutron star and black hole and is composed of strange quarks with up and down quark

matter. Numerous researchers [20,21] have conducted research regarding the structural development of quark stars.

While undertaking the exploration of compact objects, it has been observed that most of the existing interiors comprise anisotropic matter, which is currently becoming a popular subject among many astronomers. Herrera [22] argued that there must be anisotropic fluids in the structure of celestial bodies whose cores are of much lower nuclear density in comparison with their mass density. Kalam et al. [23] derived some solutions of the gravitational field equations which correspond to the various neutron stars and proved their stability and feasibility. Paul and Deb [24] presented insightful solutions for compact stars in hydrostatic equilibrium. Tangphati et al. [25] observed the interior geometry and physical properties of quark stars in Rastall theory. Salako et al. [26] looked into the effects of magnetic fields on strange quark matter in a quintessence field with the framework of Rastall theory. A detailed analysis of exotic strange quark star matter was conducted by some researchers [27,28] in a Lovelock gravity and standard theory framework with the assumption of pressure being anisotropic. Bhar [29] also built an anisotropic model of strange stars. By adopting the Krori–Barua ansatz and the MITT bag model equation of state (EOS) [20], some researchers [30,31] studied charged quark stars in Rastall theory. Mustafa et al. [31] went further to consider dust and phantom regimes. Banerjee et al. [32] used the MITT bag model and fully solved the modified Tolman–Oppenheimer–Volkoff equations in order to develop strange star models based on Rastall theory. In the same context, Sharif and Naseer [33–35] researched different kinds of anisotropic strange stars in the framework of non-minimally coupled gravity.

The MITT bag model is expected to give insights into the internal structural properties of quark stars. This model comes particularly handy in understanding the compactness values of some compact objects like *4U 1728-34*, *RXJ 185635-3754*, *Her X-1*, *4U 1820-30*, *SAX J 1808.4-3658*, *PSR 0943+10*, etc., which cannot be explained using EOS for neutron stars. The compactness of such objects can be easily understood within the context of the MITT bag model [36]. The bag constant  $\mathcal{B}$  serves to distinguish void states from the filled states as it is inversely proportional to the interior pressure of the quark stars. A couple of authors [37,38] have taken the EOS based on the MITT bag model and explored the internal fluid mechanics of quark stars. The mass of the *PSR J1614-2230* gave sufficient evidence that this was the only EOS appropriate for such a massive star. The evaluation of a star having 9.9 km of radius was utilized to calculate the mass for a couple of stars using the interpolating function [39]. Based on the Krori–Barua ansatz, Bhar [40] presented a model for a hybrid star and showed that the resulting mass function agrees with observations. Arbañil and Malheiro [41] looked at the hydrostatic equilibrium and radial instability of strange compact stars with the help of the MITT bag model to investigate the influence of anisotropy on their stability. In the same way, Deb et al. [42,43] worked on charged as well as uncharged strange stars and also developed regular solutions based on this EOS. Sharif et al. [44,45] expanded this work in deriving the solutions for anisotropic stellar bodies in the context of the MITT bag model.

Motivated by the above considerations, the present work investigates the possible presence of exotic compact stars in Rastall gravity. The study investigates various physical aspects of the sought model with the help of observational data on five known compact stars and derives numerical values for related physical parameters. The structure of the present paper is as follows. In Section 2, we derive Rastall field equations and their solutions. In Section 3, we compute the quantitative results of the Finch–Skea profile by matching the interior and exterior metrics. Section 4 presents some numerical results showing the variation of some physical properties. Ultimately, Section 5 provides the overview and the conclusions concerning the results obtained.

## 2. Rastall Field Equations and the MIT Bag Model

The field equations of Rastall theory differ from those of GR by virtue of the Rastall parameter  $\zeta$ . This parameter establishes a connection between the covariant divergence of the stress–energy tensor and that of the curvature scalar  $\mathcal{R}$  as

$$\nabla^\chi \tilde{T}_{\psi\chi} = \zeta g_{\psi\chi} \nabla^\chi \mathcal{R}. \tag{1}$$

This relation implies that the covariant divergence of the stress energy tensor  $T_{\psi\chi}$  is proportional to that of the curvature scalar, where the Rastall parameter  $\zeta$  denotes the proportionality constant. In line with the above relation, Rastall proposed a modification of the Einstein field equations, proposing a non-minimal coupling between matter and geometry as follows [1]

$$\mathcal{R}_{\psi\chi} - \frac{1}{2} \mathcal{R} g_{\psi\chi} + \zeta \mathcal{R} g_{\psi\chi} = \kappa \tilde{T}_{\psi\chi}, \tag{2}$$

where  $\zeta = \kappa \tilde{\zeta}$  denotes the Rastall dimensionless parameter and  $\mathcal{R}_{\psi\chi}, g_{\psi\chi}, \kappa$  denote the Ricci tensor, metric tensor, and coupling constant, respectively. The field equations above simplify to those of GR if  $\zeta = 0$ . In addition,  $\tilde{T}_{\psi\chi}$  denotes an energy–momentum tensor characterized by a charged anisotropic matter distribution, given by

$$\tilde{T}_{\psi\chi} = (\tilde{\rho} + \tilde{P}_t) \mathcal{W}_\psi \mathcal{W}_\chi - \tilde{P}_t g_{\psi\chi} + (\tilde{P}_r - \tilde{P}_t) \mathcal{Z}_\psi \mathcal{Z}_\chi + \frac{1}{4\pi} \left[ \frac{1}{4} g_{\psi\chi} F^{\alpha\beta} F_{\alpha\beta} - F_\psi^\alpha F_{\chi\alpha} \right]. \tag{3}$$

Here  $\tilde{\rho}, \tilde{P}_r, \tilde{P}_t, \mathcal{W}, \mathcal{Z}$  specify the energy density, radial pressure, tangential pressure, 4-velocity, and 4-vector, respectively. Considering a comoving frame, the 4-velocity and 4-vector take the form

$$\mathcal{W}^\psi = \delta_0^\psi \sqrt{g^{00}}, \quad \mathcal{Z}^\psi = \delta_1^\psi \sqrt{-g^{11}}, \tag{4}$$

and satisfy the relations  $\mathcal{W}^\psi \mathcal{W}_\psi = 1, \mathcal{W}^\psi \mathcal{Z}_\psi = 0,$  and  $\mathcal{Z}^\psi \mathcal{Z}_\psi = -1$ . The term  $F_{\alpha\beta} = \eta_{\beta,\alpha} - \eta_{\alpha,\beta}$  denotes the Maxwell field tensor with  $\eta_\beta = \eta(r) \delta_\beta^0$  as the 4-potential. This Maxwell tensor satisfies the Maxwell field equations as

$$F_{;\beta}^{\alpha\beta} = 4\pi J^\alpha, \quad F_{[\alpha\beta;\gamma]} = 0, \tag{5}$$

where  $J^\alpha$  is the 4-current, which can be written in terms of charged density  $\varphi$  as  $J^\alpha = \varphi(r) \mathcal{W}^\alpha$ .

To denote the internal geometry, we employ the metric given by

$$ds_-^2 = e^{\Phi_1(r)} dt^2 - e^{\Phi_2(r)} dr^2 - r^2 (d\theta^2 + \sin^2 \theta d\phi^2). \tag{6}$$

where the areal radius  $r$  ranges from the star center ( $r = 0$ ) to an arbitrary point ( $r = R$ ) on the surface of the star. The Maxwell field equation for our spacetime becomes

$$\eta'' + \left( \frac{2}{r} - \frac{\Phi_1'}{2} - \frac{\Phi_2'}{2} \right) \eta' = 4\pi \varphi e^{\frac{\Phi_1}{2} + \Phi_2}, \tag{7}$$

where  $' = \frac{\partial}{\partial r}$ . Upon integration of the above equation, we have

$$\eta' = \frac{e^{\frac{\Phi_1 + \Phi_2}{2}} q(r)}{r^2}, \tag{8}$$

with  $q(r) = 4\pi \int_0^r \varphi e^{\frac{\Phi_2}{2}} r^2 dr$  indicating the total charge in the interior of the sphere. By contracting the field Equation (2), we obtain

$$\mathcal{R}(4\zeta - 1) = \kappa T, \tag{9}$$

which shows that  $\zeta = \frac{1}{4}$  must be avoided. Additionally, since  $\zeta = \kappa\tilde{\zeta}$  by the Newtonian limit, we can thus write  $\kappa$  and  $\tilde{\zeta}$  in the form

$$\kappa = \frac{(4\zeta - 1)8\pi}{6\zeta - 1}, \tag{10}$$

$$\tilde{\zeta} = \frac{(6\zeta - 1)\zeta}{(4\zeta - 1)8\pi}. \tag{11}$$

It is easily observed from Equation (10) that the case  $\kappa = 8\pi$  of the GR field equations is retrieved if  $\zeta = 0$ . We also point out that the case  $\zeta = \frac{1}{6}$  cannot be considered. Using the above expression for  $\kappa$  given by Equation (10), the field equations become

$$\mathcal{R}_{\psi\chi} - \frac{1}{2}\mathcal{R}g_{\psi\chi} + \tilde{\zeta}\mathcal{R}g_{\psi\chi} = \frac{4\zeta - 1}{6\zeta - 1}8\pi\tilde{T}_{\psi\chi}. \tag{12}$$

Contracting these field equations, it follows that

$$\mathcal{R}(6\zeta - 1) = 8\pi\tilde{T}, \tag{13}$$

which implies that  $\zeta = \frac{1}{6}$  cannot be considered as implied by Equation (10). Thus, in the Newtonian limit, the cases  $\zeta = \frac{1}{4}$  and  $\zeta = \frac{1}{6}$  cannot be considered in Rastall theory.

With the metric given by Equation (6), the field Equations (12) are obtained as

$$\begin{aligned} \frac{4\zeta - 1}{6\zeta - 1} \left( 8\pi\tilde{\rho} + \frac{q^2}{r^4} \right) &= \zeta \left[ e^{-\Phi_2} \left( \Phi_1'' + \frac{\Phi_1'}{2}(\Phi_1' - \Phi_2') + \frac{2}{r}(\Phi_1' - \Phi_2') + \frac{2}{r^2} \right) - \frac{2}{r^2} \right] \\ &+ e^{\Phi_2} \left( \frac{\Phi_2'}{r} - \frac{1}{r^2} \right) + \frac{1}{r^2}, \end{aligned} \tag{14}$$

$$\begin{aligned} \frac{4\zeta - 1}{6\zeta - 1} \left( 8\pi\tilde{P}_r - \frac{q^2}{r^4} \right) &= -\zeta \left[ e^{-\Phi_2} \left( \Phi_1'' + \frac{\Phi_1'}{2}(\Phi_1' - \Phi_2') + \frac{2}{r}(\Phi_1' - \Phi_2') + \frac{2}{r^2} \right) - \frac{2}{r^2} \right] \\ &+ e^{\Phi_2} \left( \frac{\Phi_1'}{r} + \frac{1}{r^2} \right) - \frac{1}{r^2}, \end{aligned} \tag{15}$$

$$\begin{aligned} \frac{4\zeta - 1}{6\zeta - 1} \left( 8\pi\tilde{P}_t + \frac{q^2}{r^4} \right) &= -\zeta \left[ e^{-\Phi_2} \left( \Phi_1'' + \frac{\Phi_1'}{2}(\Phi_1' - \Phi_2') + \frac{2}{r}(\Phi_1' - \Phi_2') + \frac{2}{r^2} \right) - \frac{2}{r^2} \right] \\ &+ e^{-\Phi_2} \left[ \frac{\Phi_1''}{2} + \frac{\Phi_1'^2}{4} - \frac{\Phi_1'\Phi_2'}{4} + \frac{\Phi_1' - \Phi_2'}{2r} \right]. \end{aligned} \tag{16}$$

The aforementioned system presents six variables  $(\tilde{\rho}, \Phi_1, \Phi_2, \tilde{P}_r, \tilde{P}_t, q)$  in three equations, thus requiring three constraints for the system to be closed. Equations of state, which are different limitations that relate the thermodynamic parameters of fluid states, are essential for the study of the physical characteristics of compact objects. Stellar objects with a mass exceeding 8 but less than 20 times that of the sun will classically end up as neutron stars, which happen to be the most interesting objects in the universe. Such neutron stars, depending on the density of the stars, may further be classified into either quark stars or black holes [37]. It is important to understand that these stars, even though they are incredibly small, are able to produce very vicious gravitational fields due to the extreme densities obtained within them. To investigate the inner structure of strange stars, we will make use of the MIT bag model EOS. This is a model that links state variables of compact star configurations and is necessary for distinguishing the most essential aspects of quark stars.

The MIT bag EOS is given by [20]

$$3\tilde{P}_r = (\tilde{\rho} - 4B), \tag{17}$$

where  $B$  denotes the bag constant. The value of this constant is not entirely arbitrary, as it is generally accepted to fall within the range of  $57 \leq B \leq 92 \text{ MeV}/f m^3$  [46]. Using this EOS together with the metric coefficients of the Finch–Skea spacetime [47], given by

$$e^{\Phi_1(r)} = \left(A + \frac{1}{2}Br\sqrt{Cr^2}\right)^2, \quad e^{\Phi_2(r)} = 1 + Cr^2, \tag{18}$$

where  $A, B, C$  are constants and can be determined through the matching conditions at the boundary. We obtain the following expressions for the matter variables in the field Equations (14)–(16):

$$\tilde{\rho} = -\frac{(6\zeta - 1)\left(-\frac{3C}{(Cr^2+1)^2} - \frac{6B\sqrt{Cr^2}}{r(Cr^2+1)(Br\sqrt{Cr^2}+2A)} + \frac{16\pi B(1-4\zeta)}{6\zeta-1}\right)}{16\pi(4\zeta - 1)}, \tag{19}$$

$$\tilde{P}_r = \frac{(6\zeta - 1)\left(B\sqrt{Cr^2}(3Cr^2 + 2) + 2ACr\right)}{16\pi(4\zeta - 1)r(Cr^2 + 1)^2\left(Br\sqrt{Cr^2} + 2A\right)} - B, \tag{20}$$

$$\begin{aligned} \tilde{P}_t = & \frac{1}{16\pi(4\zeta - 1)\sqrt{Cr^2}(Cr^2 + 1)^2\left(Br\sqrt{Cr^2} + 2A\right)} \left[ BCr \left[ Cr^2 \right. \right. \\ & \times \left[ 2C(4\zeta - 1)r^2\left(8\pi Br^2 + 6\zeta - 1\right) + 32\pi B(4\zeta - 1)r^2 - 48\zeta^2 + 38\zeta \right. \\ & \left. \left. - 5\right] + 2\left(8\pi B(4\zeta - 1)r^2 + 6\zeta(11 - 24\zeta) - 7\right) \right] + 2A\sqrt{Cr^2} \left[ C \right. \\ & \times \left[ 2C(4\zeta - 1)r^2\left(8\pi Br^2 + 6\zeta - 1\right) + 16\left(2\pi B(4\zeta - 1)r^2 + 9\zeta^2\right) \right. \\ & \left. \left. - 54\zeta + 5\right] + 16\pi B(4\zeta - 1) \right] \left. \right]. \end{aligned} \tag{21}$$

Additionally, the charge parameter  $q$  is obtained as

$$\begin{aligned} q^2 = & \frac{-1}{2(4\zeta - 1)(Cr^2 + 1)^2\left(2A\sqrt{Cr^2} + BCr^3\right)\left(2A + r\sqrt{Cr^2}\right)} \left[ r^4 \left[ 4A^2\sqrt{Cr^2} \right. \right. \\ & \times \left[ 2C^2r^2\left(8\pi B(4\zeta - 1)r^2 + 4\zeta(3\zeta - 2) + 1\right) + C(4\zeta - 1)\left(32\pi Br^2 + 18\zeta - 3\right) \right. \\ & \left. \left. + 16\pi B(4\zeta - 1) \right] + 4(ABC)r \left[ 16\pi B(4\zeta - 1)\left(Cr^3 + r\right)^2 + (6\zeta - 1) \right. \right. \\ & \times \left[ 2Cr^2\left(C(2\zeta - 1)r^2 + 2\zeta\right) - 12\zeta + 3 \right] + B^2\left(Cr^2\right)^{3/2} \left[ 2C^2r^4 \left[ 8\pi B(4\zeta - 1)r^2 \right. \right. \\ & \left. \left. + 4\zeta(3\zeta - 2) + 1 \right] + Cr^2\left(32\pi B(4\zeta - 1)r^2 - 24\zeta^2 + 22\zeta - 3\right) + 2(4\zeta - 1) \right. \\ & \left. \left. \times \left(8\pi Br^2 - 18\zeta + 3\right) \right] \right] \left. \right]. \end{aligned} \tag{22}$$

### 3. Junction Conditions

The junction conditions define the conditions for fulfilling the smooth matching of the physical properties at the boundary of the inner and outer regions of a compact object. Such fundamental aspects as the nature of the interior spacetime geometry (dynamic or

static) and/or the presence of an electromagnetic field, dictate the choice of the exterior geometry to be selected for matching. Since the inner geometry is dictated by the presence of charge, the external spacetime suitable for this case is the Reissner–Nordström (RN) metric. The outer RN metric is given by

$$ds_+^2 = \left(1 - \frac{2\tilde{M}}{r} + \frac{\tilde{Q}^2}{r^2}\right) dt^2 - \left(1 - \frac{2\tilde{M}}{r} + \frac{\tilde{Q}^2}{r^2}\right)^{-1} dr^2 - r^2(d\theta^2 + \sin^2\theta d\phi^2), \quad (23)$$

where  $\tilde{M}$  and  $\tilde{Q}$  denote the mass and charge at the boundary, where  $r = \mathcal{H}$ . This equality results from the continuity of the first fundamental form at the boundary of the compact object, where the interior and exterior geometries merge. Here,  $r$  and  $\mathcal{H}$  denote the radii of the interior and exterior geometries, respectively. This inequality thus implies that at the boundary of the compact objects, the radii of the interior and exterior geometries are equal as stipulated by the junction conditions.

Applying the Darmois junction conditions, we obtain the following constraints to enhance smooth matching at the surface:

$$g_{tt} : \left(A + \frac{1}{2}B\mathcal{H}\sqrt{C\mathcal{H}^2}\right)^2 = 1 - \frac{2\tilde{M}}{\mathcal{H}} + \frac{\tilde{Q}^2}{\mathcal{H}^2}, \quad (24)$$

$$g_{rr} : \frac{1}{1 + C\mathcal{H}^2} = 1 - \frac{2\tilde{M}}{\mathcal{H}} + \frac{\tilde{Q}^2}{\mathcal{H}^2}, \quad (25)$$

$$g_{tt,r} : B\left(2A\sqrt{C\mathcal{H}^2} + B\mathcal{H}^3\right) = \frac{2(\tilde{M}\mathcal{H} - \tilde{Q}^2)}{\mathcal{H}^3}. \quad (26)$$

Solving the above system simultaneously, we obtain the Finch–Skea constants ( $A, B, C$ ) as

$$A = \frac{\sqrt{-\frac{\tilde{Q}^2 - 2\tilde{M}\mathcal{H}}{-2\tilde{M}\mathcal{H} + \tilde{Q}^2 + \mathcal{H}^2}} (\mathcal{H}(2\mathcal{H} - 5\tilde{M}) + 3\tilde{Q}^2)}{2\mathcal{H}\sqrt{2\tilde{M}\mathcal{H} - \tilde{Q}^2}}, \quad (27)$$

$$B = \frac{\tilde{M}\mathcal{H} - \tilde{Q}^2}{\mathcal{H}^2\sqrt{2\tilde{M}\mathcal{H} - \tilde{Q}^2}}, \quad (28)$$

$$C = \frac{1}{-2\tilde{M}\mathcal{H} + \tilde{Q}^2 + \mathcal{H}^2} - \frac{1}{\mathcal{H}^2}. \quad (29)$$

The experimental data, including the masses and radii of five different strange stars, namely *Her X-1* [48], *SAX J 1808.4-3658* [49], *PSR J038-0842* [48], *LMC X-4* [50], and *SMC X-1* [50], are utilized. This information is provided in Table 1, where we also calculate the mass–radius ratio for each star as a dimensionless quantity. We find that these computed ratios comply with the limit  $\frac{\tilde{M}}{2\tilde{H}} < \frac{2}{9}$  as suggested by Buchdahl [51]. Additionally, in Table 2, we present the values of the Finch–Skea triplet ( $A, B, C$ ), as well as  $\frac{\tilde{Q}^2}{\mathcal{H}^2}$ .

**Table 1.** Experimental data of five strange stars.

Star Models	Mass ( $M_\odot$ )	$\mathcal{G}$ (km)	$\frac{\tilde{M}}{\mathcal{H}}$
Her X-1	0.85	8.1	0.154679
SAX J 1808.4-3658	1.44	7.07	0.300221
PSR J038-0842	2.1	10.06	0.307694
LMC X-4	1.29	8.831	0.215316
SMC X-1	1.04	9.34	0.164128

**Table 2.** Values of Finch–Skea triplets ( $A, B, C$ ) and  $\frac{Q^2}{H^2}$ .

Star Models	A	B	C	$\frac{Q^2}{H^2}$
Her X-1	0.738761	0.0342317	0.00680767	0.000609663
SAX J 1808.4-3658	0.396133	0.0546911	0.0299642	0.000800242
PSR J038-0842	0.372864	0.0389518	0.0157835	0.000395243
LMC X-4	0.612632	0.0370883	0.00967802	0.000512909
SMC X-1	0.720066	0.0306069	0.00559002	0.000458528

### 4. Physical Analysis

This study investigates the various structural properties of strange stars using an anisotropic model under Rastall gravity. Following the information from Table 1, the graphical representations of different matter parameters are analyzed. The analysis covers the study of the properties of quark stars, in particular, the appearance and the possible limitations of the stars metric potentials, the energy density distribution, and the anisotropic stress. Energy constraints, compactness, and surface redshift are also considered. Their stability is also studied. A regular solution guarantees that the components of the considered metric do not contain singularities and are increasing and positive everywhere. The metric components, as shown in Equation (18), depend only on the Finch–Skea parameters for which the values are provided in Table 2. We include the effect of an electric field by adopting  $Q = 0.2, 0.7$  and the values of the Rastall parameter as  $\zeta = 0.255, 0.259$ , which are represented by thick and broken lines, respectively. These values of the Rastall parameter are chosen to be of the order  $10^{-3}$  in line with the results from [52], where 118 galaxy–galaxy strong gravitational lensing systems were used to constrain the Rastall dimensionless parameter. Where appropriate, we set  $B = 60 \text{ MeV}/\text{fm}^3$  for the bag constant.

The considered quark candidates, *Her X-1*, *SAX J 1808.4-3658*, *PSR J038-0842*, *LMC X-4*, and *SMC X-1*, are denoted by the colors blue, brown, green, red, and black, respectively. The metric functions are shown in Figures 1 and 2 for the cases  $Q = 0.2$  and  $Q = 0.7$ , respectively, and serve to demonstrate the physical plausibility of the solution obtained. However, we observe no impact of the increment on the charge.

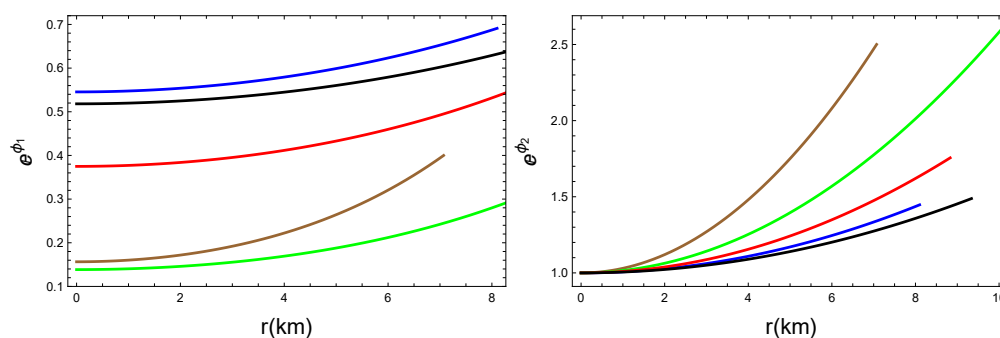


**Figure 1.** Plots of metric functions against  $r$  for  $Q = 0.2$ . (The colors blue, brown, green, red, and black, denote the considered quark candidates, *Her X-1*, *SAX J 1808.4-3658*, *PSR J038-0842*, *LMC X-4*, and *SMC X-1*, respectively).

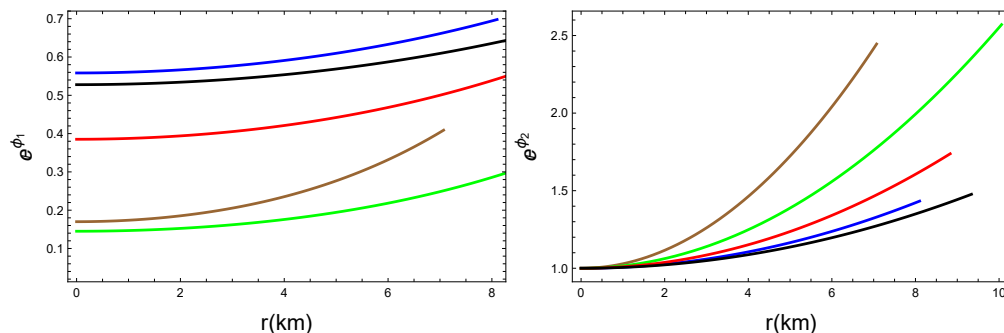


**Figure 2.** Plots of metric functions against  $r$  for  $\tilde{Q} = 0.7$ . (The colors blue, brown, green, red, and black, denote the considered quark candidates, Her X-1, SAX J 1808.4-3658, PSR J038-0842, LMC X-4, and SMC X-1, respectively).

4.1. Matter Variables

In any particular geometric configuration, matter becomes centralized around the core. Thus, a physical solution can be found only if the central part possesses maximal values of the matter parameters (such as density or pressure), which decrease towards the surface. Given the anisotropic configuration of the considered fluid, we essentially consider three main parameters, viz.  $\tilde{\rho}$ ,  $\tilde{P}_r$ , and  $\tilde{P}_t$ . As presented in Figures 3 and 4, these parameters satisfy the aforementioned requirements. We notice that the core density is slightly higher for a smaller value of  $\tilde{Q}$  and thus deduce that the density has an inverse correlation to the electric field. The same trend can be observed in relation to  $\tilde{P}_r$  as well. For comparison purposes, we plot the GR case ( $\zeta = 0$ ) for the effective parameters in Figure 5, where it is observed that these parameters attain higher values at the core compared to the case of Rastall gravity ( $\zeta \neq 0$ ).

In addition, we check the regularity of these matter parameters with the help of the conditions  $\frac{d\tilde{\rho}}{dr} < 0$ ,  $\frac{d\tilde{P}_r}{dr} < 0$ ,  $\frac{d\tilde{P}_t}{dr} < 0$ . Figures 6 and 7 show that the properties of the matter obey these regularity principles, which means that within this approach, matter is postulated to be highly anisotropic, yet also very dense. It is also observed that smaller values of the Rastall parameter leads to the formation of a denser core and higher core radial pressure.

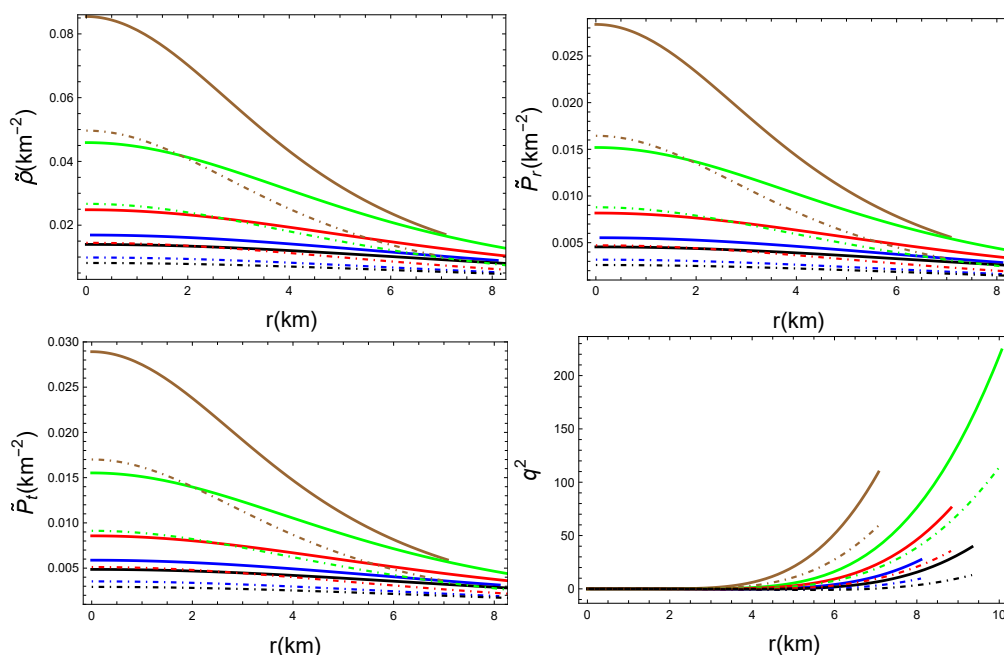


**Figure 3.** Plots of  $\tilde{\rho}$ ,  $\tilde{P}_r$ ,  $\tilde{P}_t$  and  $q^2$  against  $r$  for  $\zeta = 0.255$  (thick),  $0.259$  (broken) and  $\tilde{Q} = 0.2$ . (The colors blue, brown, green, red, and black, denote the considered quark candidates, Her X-1, SAX J 1808.4-3658, PSR J038-0842, LMC X-4, and SMC X-1, respectively).

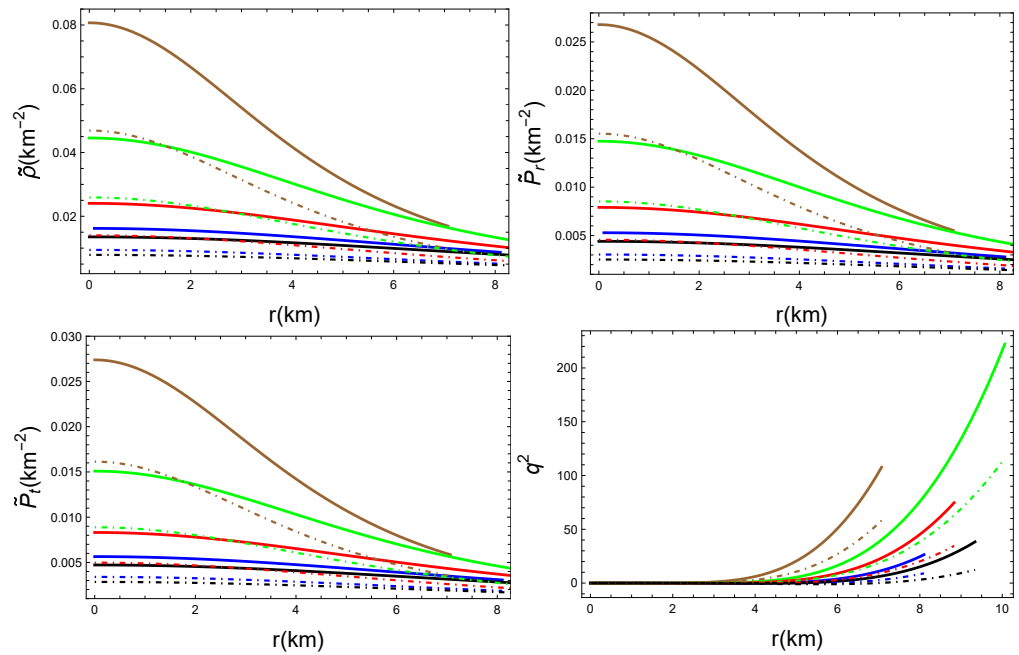


**Figure 4.** Plots of  $\tilde{\rho}$ ,  $\tilde{P}_r$ ,  $\tilde{P}_t$  and  $q^2$  against  $r$  for  $\zeta = 0.255$  (thick),  $0.259$  (broken) and  $0.7$ . (The colors blue, brown, green, red, and black, denote the considered quark candidates, Her X-1, SAX J 1808.4-3658, PSR J038-0842, LMC X-4, and SMC X-1, respectively).

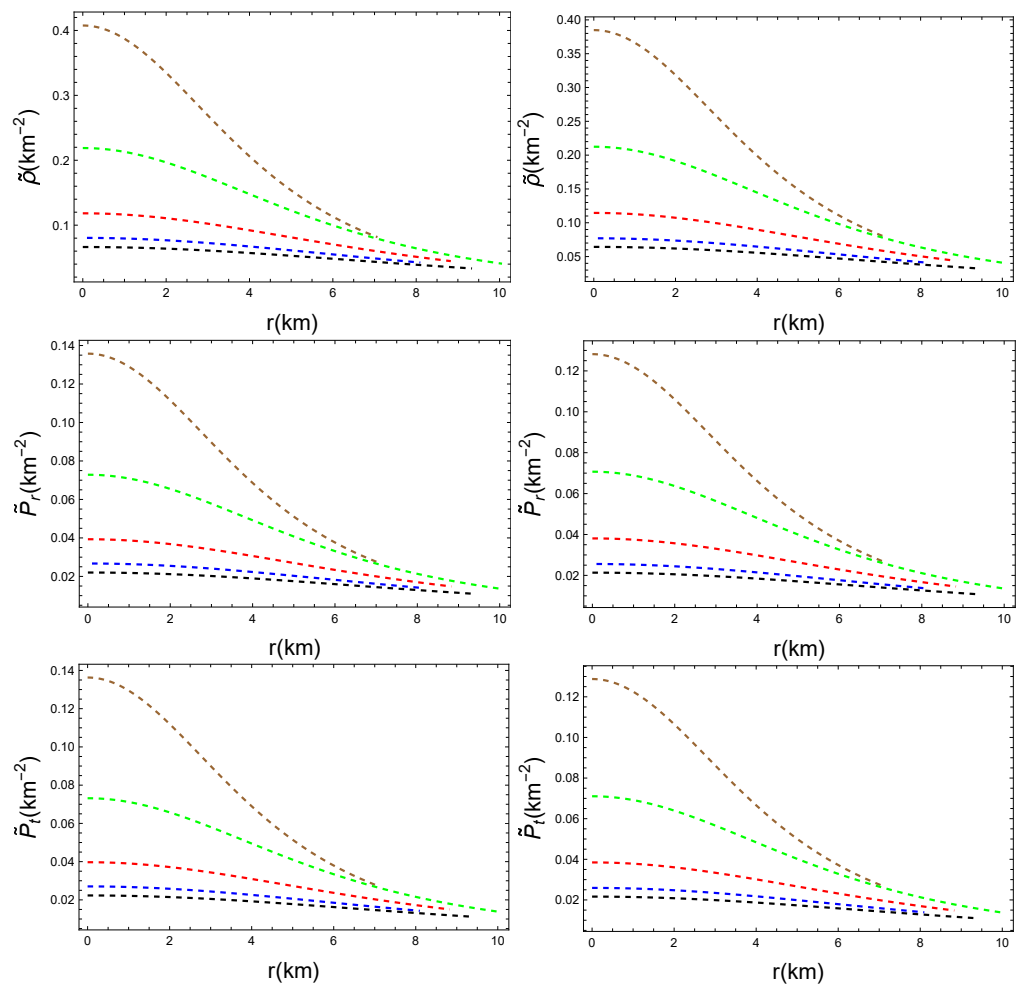


**Figure 5.** Plots of  $\tilde{\rho}$ ,  $\tilde{P}_r$ ,  $\tilde{P}_t$  against  $r$  for  $\zeta = 0$  and  $0.7$  (left),  $0.7$  (right). (The colors blue, brown, green, red, and black, denote the considered quark candidates, Her X-1, SAX J 1808.4-3658, PSR J038-0842, LMC X-4, and SMC X-1, respectively).

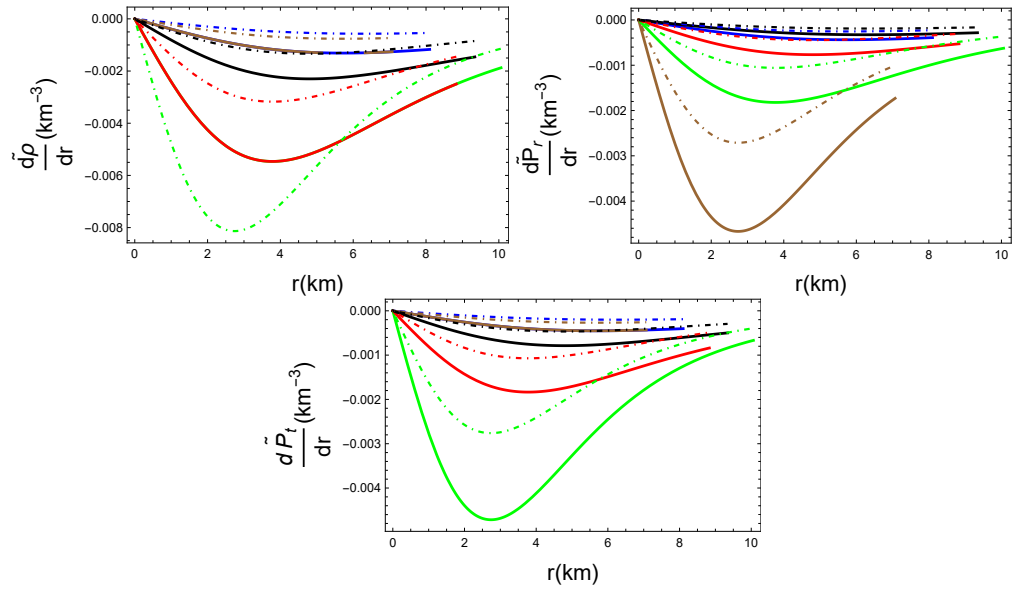


**Figure 6.** Plots of  $\frac{d\bar{\rho}}{dr}$ ,  $\frac{d\bar{P}_r}{dr}$ , and  $\frac{d\bar{P}_t}{dr}$  against  $r$  for  $\zeta = 0.255$  (thick),  $0.259$  (broken) and  $\tilde{Q} = 0.2$ . (The colors blue, brown, green, red, and black, denote the considered quark candidates, Her X-1, SAX J 1808.4-3658, PSR J038-0842, LMC X-4, and SMC X-1, respectively).

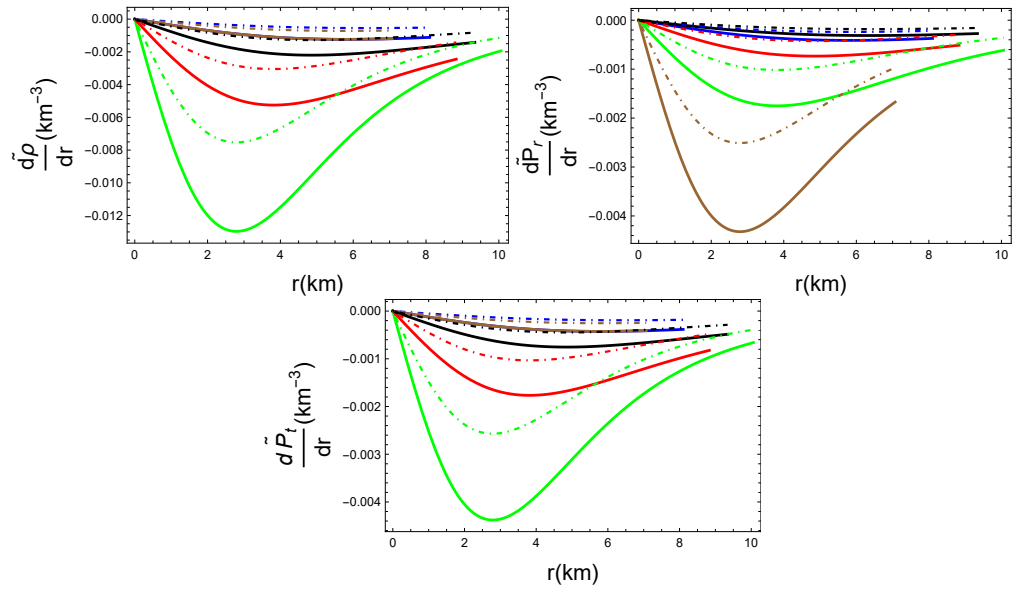


**Figure 7.** Plots of  $\frac{d\bar{\rho}}{dr}$ ,  $\frac{d\bar{P}_r}{dr}$ , and  $\frac{d\bar{P}_t}{dr}$  against  $r$  for  $\zeta = 0.255$  (thick),  $0.259$  (broken) and  $\tilde{Q} = 0.7$ . (The colors blue, brown, green, red, and black, denote the considered quark candidates, Her X-1, SAX J 1808.4-3658, PSR J038-0842, LMC X-4, and SMC X-1, respectively).

#### 4.2. Pressure Anisotropy

The pressure anisotropy  $\tilde{\Delta}$  is given by  $\tilde{\Delta} = \tilde{P}_t - \tilde{P}_r$  and can be evaluated using Equations (20) and (21) as

$$\begin{aligned} \tilde{\Delta} = & \frac{1}{8\pi(Cr^3 + r)^2 \left( 4(A + Br\sqrt{Cr^2}) + B^2Cr^4 \right)} \left[ r \left[ 4A^2r \left[ C \left[ r^2 \left[ C \right. \right. \right. \right. \right. \right. \right. \right. \\ & \times \left( 16\pi Br^2 + 6\zeta - 1 \right) + 32\pi B \left. \right] + 18\zeta - 3 \left. \right] + 16\pi B \left. \right] + 4AB\sqrt{Cr^2} \\ & \times \left( r^2(Cr^2 + 1) \left( C(16\pi Br^2 + 6\zeta - 1) + 16\pi B \right) - 18\zeta + 3 \right) + AB^2Cr^3 \\ & \times \left[ r^2 \left( C \left( r^2 \left( C(16\pi Br^2 + 6\zeta - 1) + 32\pi B \right) - 6\zeta + 1 \right) + 16\pi B \right) - 36\zeta \right. \\ & \left. + 6 \right] \right] \right]. \end{aligned} \tag{30}$$

The distinguishing feature of anisotropic pressure is the difference between the tangential and radial components. If the tangential stress is greater than the radial stress of the material ( $\tilde{P}_t > \tilde{P}_r$ ), it is an indication that the material is under an outward force, while if it is the other way around ( $\tilde{P}_r > \tilde{P}_t$ ) then it is a force directed inwards. A factor of positive anisotropic pressure in such bodies produces an external force that counteracts the inward gravitational pull in such spheres in order to ensure that balance is achieved. The distribution of anisotropic pressure in the selected models of the quark stars is presented in Figure 8. It is observed that  $\tilde{\Delta}$  is smooth and decreases towards the surface but remains positive at all times, which suggests that there is a force that works towards building such heavy stellar structures.

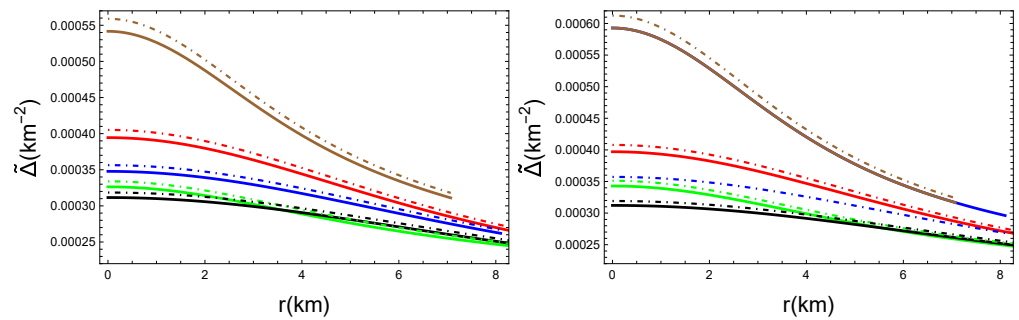


**Figure 8.** Plots of anisotropic pressure ( $\tilde{\Delta}$ ) against  $r$  for  $\zeta = 0.255$  (thick),  $0.259$  (broken) and  $\tilde{Q} = 0.2$  (left),  $= 0.7$  (right). (The colors blue, brown, green, red, and black, denote the considered quark candidates, Her X-1, SAX J 1808.4-3658, PSR J038-0842, LMC X-4, and SMC X-1, respectively).

### 4.3. Mass, Compactness, and Surface Redshift

In order to calculate the mass of a sphere, its energy density can be taken into consideration by using the equation

$$m(r) = 4\pi \int_0^r \tilde{\rho} r^2 dr, \tag{31}$$

where  $\tilde{\rho}$  is defined in Equation (19). Figures 9 and 10 (corresponding to  $\tilde{Q} = 0.2$  and  $\tilde{Q} = 0.7$ , respectively) show that the mass function starts at zero in the core and increases steadily towards the surface. Additionally, we study the compactness of the sphere,  $\sigma(r) = \frac{m(r)}{r}$ , and the surface redshift,  $Z_s(r) = \frac{1}{\sqrt{1-2\sigma(r)}} - 1$ . How properly an object mass is distributed within a given radius is called the compactness of the object, and it is an important factor in the assessment of the strength of the gravitational field along the surface of a star. Changes in the wavelengths of electromagnetic radiations emitted from the surface of a compact object are shown by the surface redshift,  $Z_s(r)$ . The strong field in the vicinity of the surface reduces the energy of the emitted radiation causing a redshift of the radiation, meaning an increase in wavelength. Photons that are generated from the central core tend to travel through denser sections of the core, which results in them losing some energy

due to scattering. On the other hand, the surface, where the emission occurs, is occupied with less dense material, which lessens the amount of scattering and therefore the loss of energy. For a physically viable configuration to exist, the following conditions must hold  $\sigma < \frac{4}{9}$  [51] and  $Z_s \leq 5.2$  [53]. The relations between the compression of liquid and surface redshift as shown in Figures 9 and 10 suggest that the limits required by the aforementioned parameters are observed in this model.

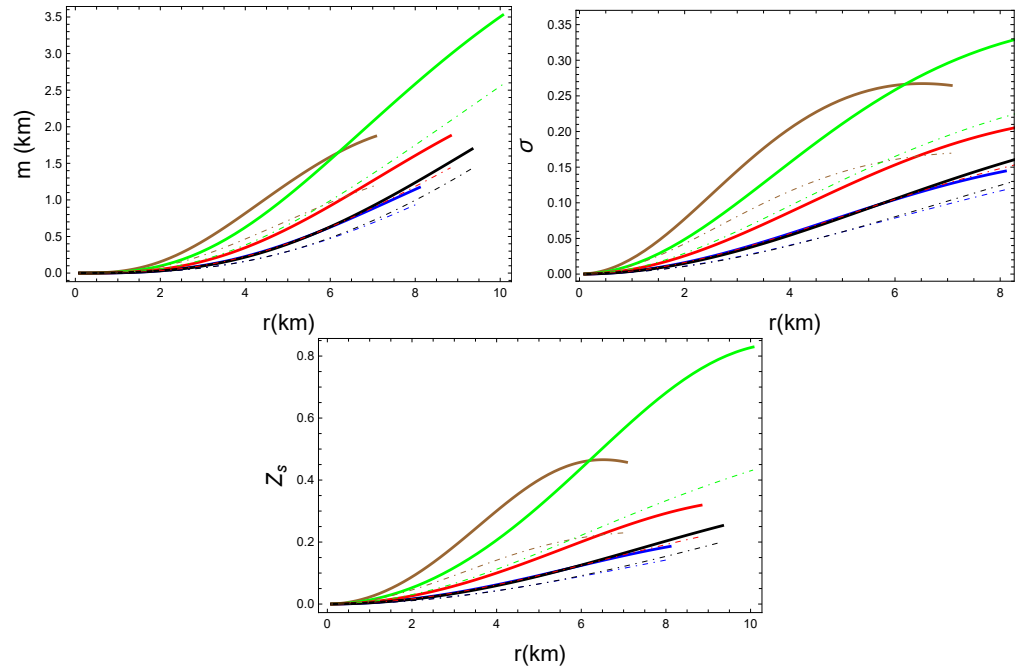


**Figure 9.** Plots of  $m(r)$ ,  $\sigma$ , and  $Z_s$  against  $r$  for  $\zeta = 0.255$  (thick),  $0.259$  (broken) and  $\tilde{Q} = 0.2$ . (The colors blue, brown, green, red, and black, denote the considered quark candidates, Her X-1, SAX J 1808.4-3658, PSR J038-0842, LMC X-4, and SMC X-1, respectively).

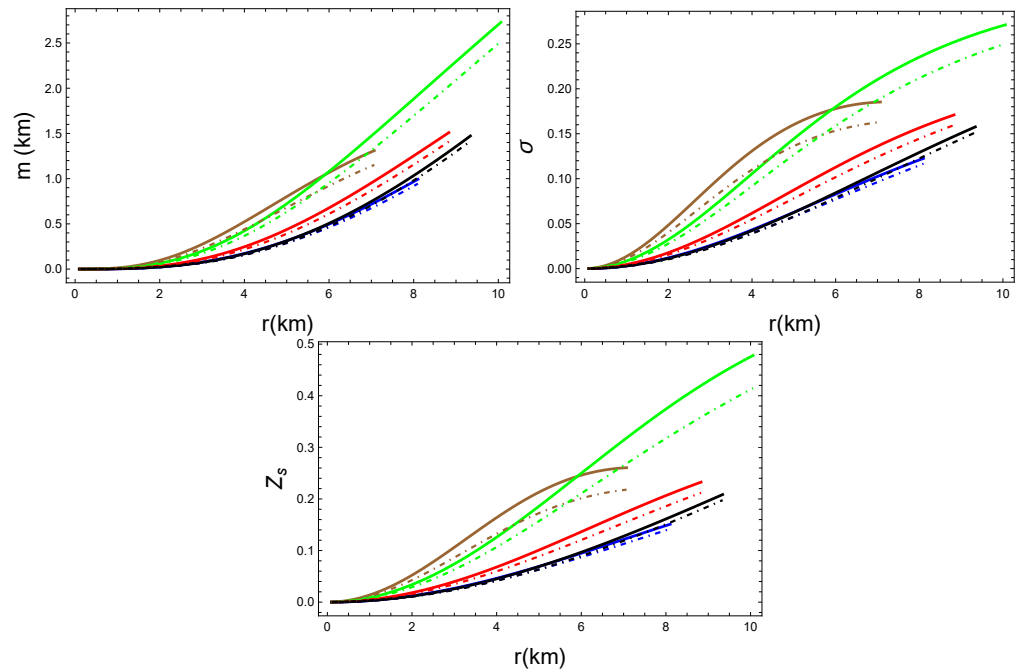


**Figure 10.** Plots of  $m(r)$ ,  $\sigma$ , and  $Z_s$  against  $r$  for  $\zeta = 0.255$  (thick),  $0.259$  (broken) and  $\tilde{Q} = 0.7$ . (The colors blue, brown, green, red, and black, denote the considered quark candidates, Her X-1, SAX J 1808.4-3658, PSR J038-0842, LMC X-4, and SMC X-1, respectively).

#### 4.4. Energy Conditions

Astrophysics has a procedure to determine the kind of matter that makes up the body of any given heavenly body. These are given by a known set of constraints, termed as energy conditions. Such restrictions put in place are important to understand the features of such bodies and how they act. These conditions (classified as dominant, strong, null, and weak energy conditions) help to define the region occupied by normal and strange matter in a given geometry. The fulfillment of these conditions, which are functions of the physical quantities  $\tilde{\rho}_r, \tilde{P}_t$  and  $\tilde{\rho}$ , is indicative of the existence of regular matter in a correlated star. Also, these bounds serve the purpose of determining whether certain proposed models are realistic in different theories of gravity. It is necessary that the relevant physical parameters fulfill certain limits to enable ordinary matter content in a given geometric configuration. These criteria can be categorized as follows:

$$\begin{aligned} \tilde{\rho} + \frac{q^2}{8\pi r^4} &\geq 0, & \tilde{\rho} + \tilde{P}_r &\geq 0, \\ \tilde{\rho} - \tilde{P}_r + \frac{q^2}{4\pi r^4} &\geq 0, & \tilde{\rho} - \tilde{P}_t &\geq 0, \\ \tilde{\rho} + \tilde{P}_t + \frac{q^2}{4\pi r^4} &\geq 0, & \tilde{\rho} + \tilde{P}_r + 2\tilde{P}_t + \frac{q^2}{4\pi r^4} &\geq 0. \end{aligned}$$

Figures 11 and 12 illustrate these conditions corresponding to  $\tilde{Q} = 0.2$  and  $\tilde{Q} = 0.7$ , respectively. It is shown that these conditions are satisfied, implying the presence of ordinary matter in the interior of the considered stellar configurations.

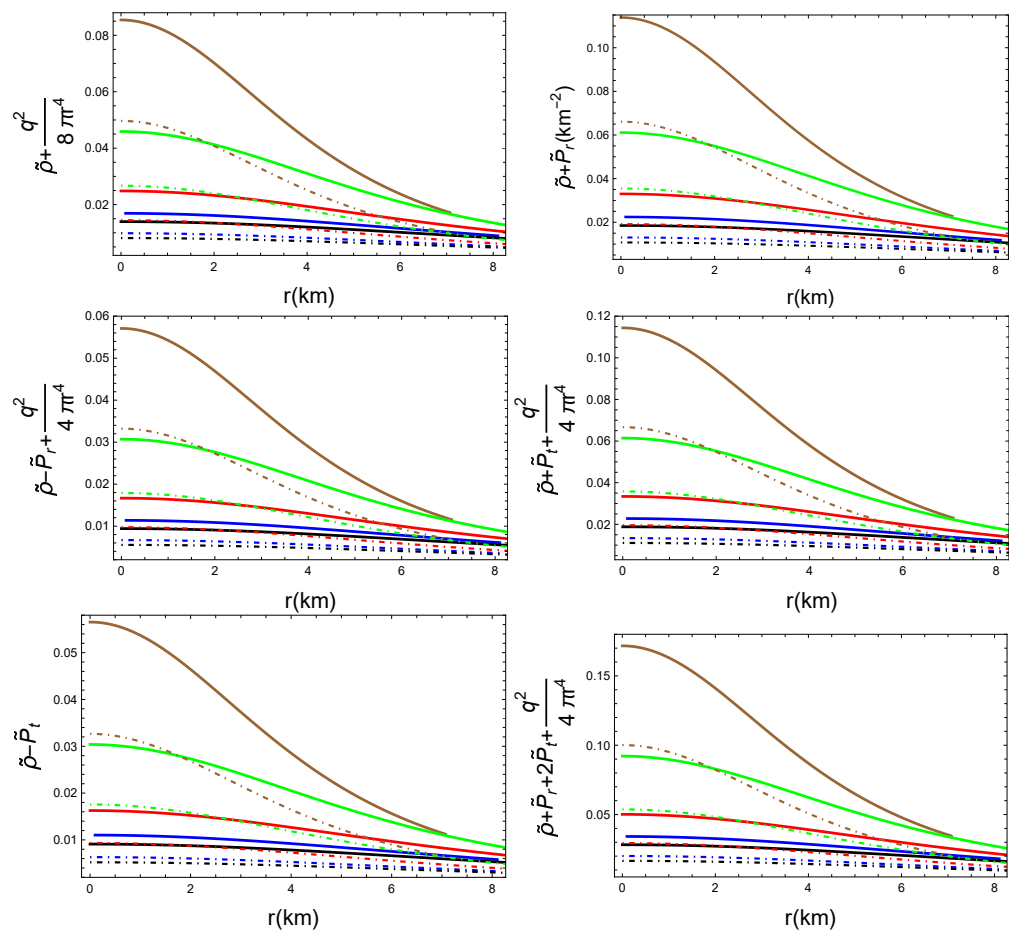


**Figure 11.** Graphs of energy bounds against  $r$  for  $\zeta = 0.255$  (thick),  $0.259$  (broken) and  $\tilde{Q} = 0.2$ . (The colors blue, brown, green, red, and black, denote the considered quark candidates, Her X-1, SAX J 1808.4-3658, PSR J038-0842, LMC X-4, and SMC X-1, respectively).

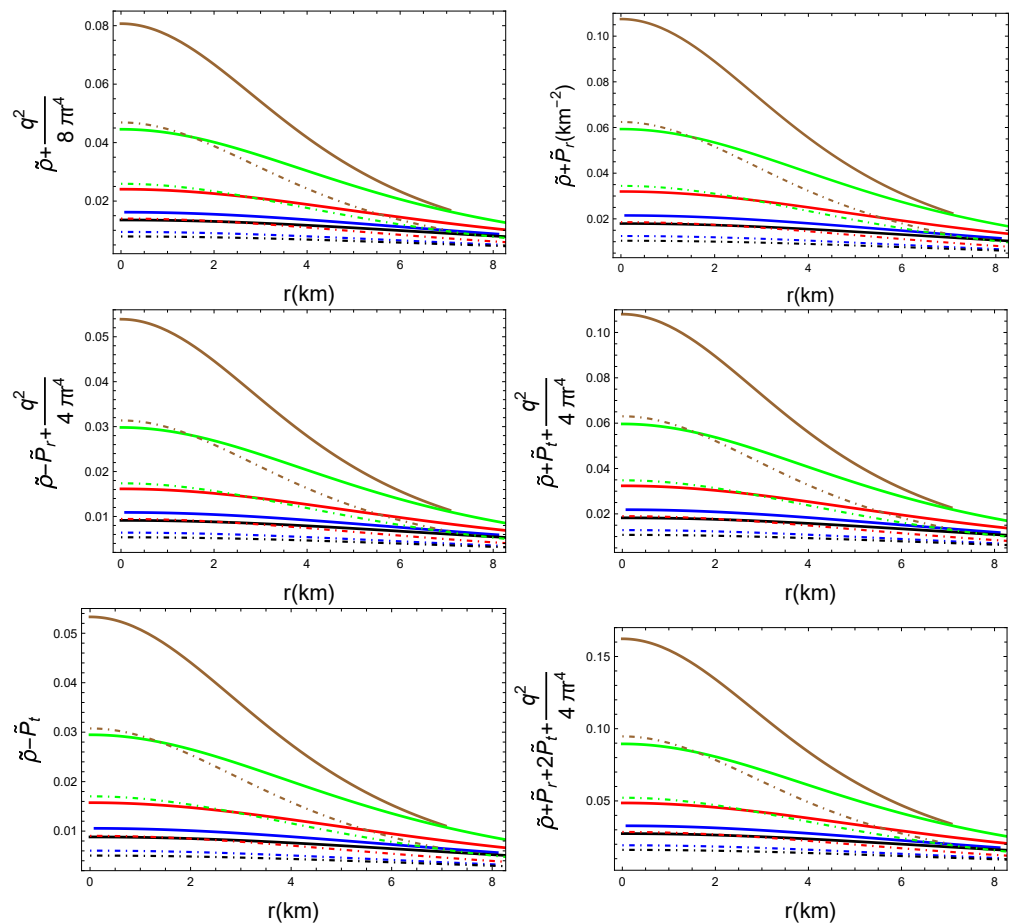


**Figure 12.** Graphs of energy bounds against  $r$  for  $\zeta = 0.255$  (thick),  $0.259$  (broken) and  $\tilde{Q} = 0.7$ . (The colors blue, brown, green, red, and black, denote the considered quark candidates, Her X-1, SAX J 1808.4-3658, PSR J038-0842, LMC X-4, and SMC X-1, respectively).

#### 4.5. Stability

The stability of compact star has drawn the attention of astrophysicists, as it helps to create physically realistic models of such objects. It is captivating to study those huge celestial masses that can maintain their stable behavior irrespective of the changes made to their environment, hence the importance of studying their structural stability. In this regard, with Rastall theory taken into account, we use two different methods for the stability analysis of the compact stars.

Firstly, we employ the cracking process attributed to Herrera [22]. With this criterion, stability is guaranteed if the requirement  $0 \leq |V_{st}^2 - V_{sr}^2| \leq 1$  holds, wherein  $V_{st}^2 = \frac{d\tilde{P}_t}{d\tilde{\rho}}$  is understood as the tangential sound speed while  $V_{sr}^2 = \frac{d\tilde{P}_r}{d\tilde{\rho}}$  is the radial sound speed. In Figure 13, the Herrera cracking condition is presented, showing that the configurations remain stable for all the parameters under consideration. Additionally, we investigate the stability of the proposed models via the causality conditions with which stability necessitates that  $0 \leq V_{sr}^2, V_{st}^2 \leq 1$  [54]. The result of this test shown in Figure 14, depicts a stable configuration.

Furthermore, we investigate the stability using the adiabatic index  $\Gamma$ , which is a fundamental tool for the stability analysis of self-gravitating objects. This approach necessitates that the adiabatic index remains greater than  $\frac{4}{3}$  across the entire model for a stable system [55]. With this parameter, the criterion for stability is  $\Gamma > \frac{4}{3}$ , where

$$\Gamma = \left( \frac{\tilde{\rho} + \tilde{P}_r}{\tilde{P}_r} \right) \frac{d\tilde{P}_r}{d\tilde{\rho}}. \tag{32}$$

We plot the adiabatic index in Figure 15, from which we deduce the stability of all the considered configurations. Given that these methods are widely accepted and have been rigorously applied in this study, we contend that they are sufficient to substantiate the stability of our models. While additional graphical representations may provide a visual confirmation of the results, the detailed analysis already presented in the manuscript confirms that the necessary stability criteria are fully satisfied. To enhance a comparative analysis, we also investigate the stability of the model for the GR case as shown in Figure 16, where a stable configuration is also deduced.

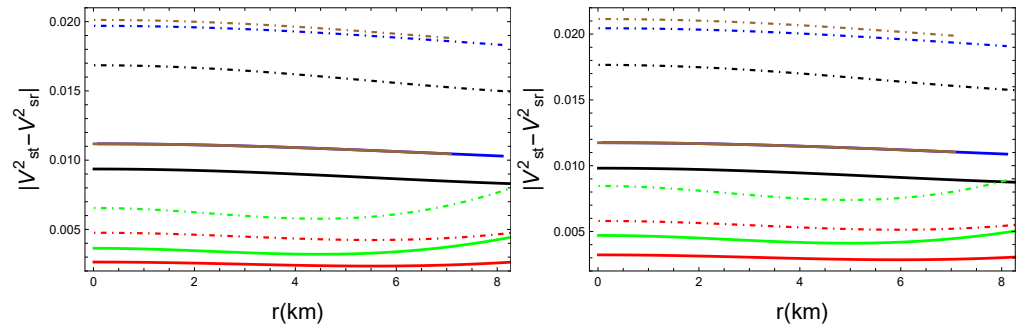


**Figure 13.** Plots of  $|V_{st}^2 - V_{sr}^2|$  against  $r$  for  $\zeta = 0.255$  (thick),  $0.259$  (broken) and  $\tilde{Q} = 0.2$  (left),  $0.7$  (right). (The colors blue, brown, green, red, and black, denote the considered quark candidates, Her X-1, SAX J 1808.4-3658, PSR J038-0842, LMC X-4, and SMC X-1, respectively).

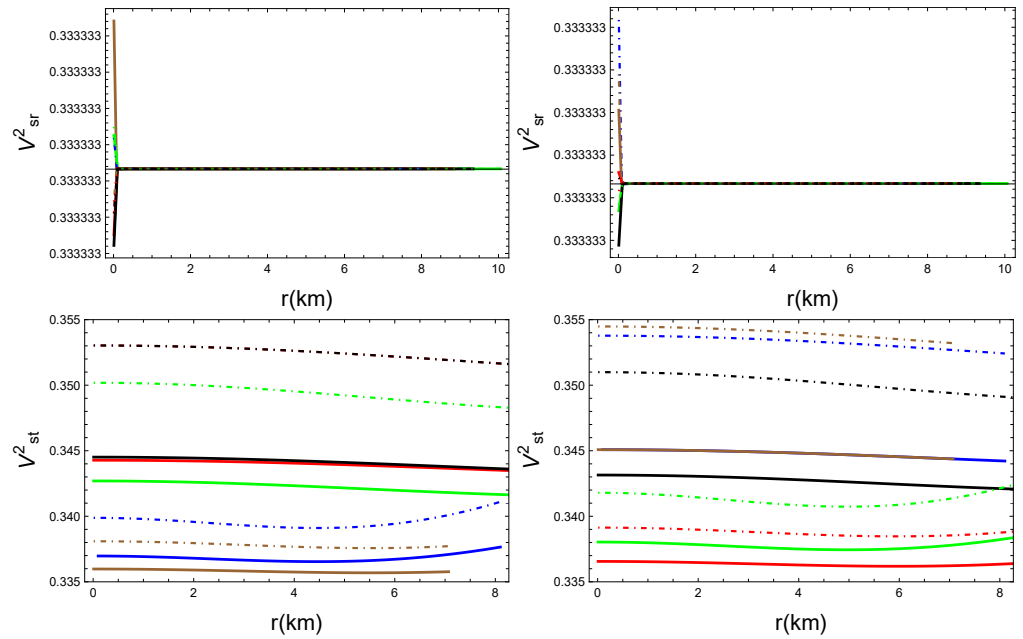


**Figure 14.** Plots of  $V_{sr}^2$  and  $V_{st}^2$  against  $r$  for  $\zeta = 0.255$  (thick),  $0.259$  (broken) and  $\tilde{Q} = 0.2$  (left),  $0.7$  (right). (The colors blue, brown, green, red, and black, denote the considered quark candidates, Her X-1, SAX J 1808.4-3658, PSR J038-0842, LMC X-4, and SMC X-1, respectively).

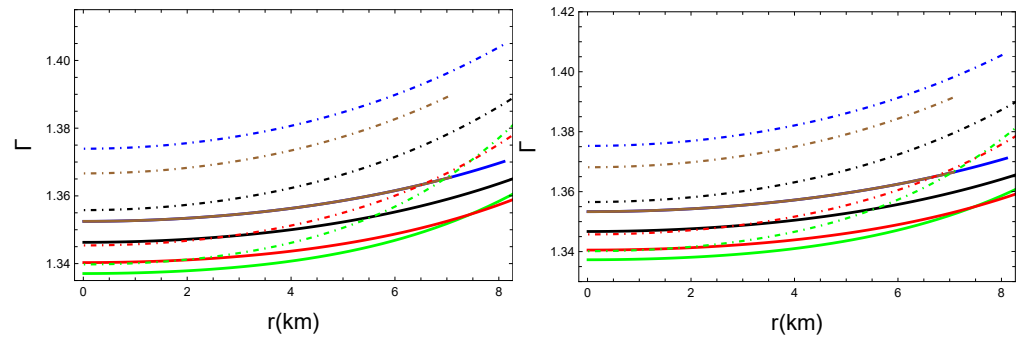


**Figure 15.** Plots of  $\Gamma$  against  $r$  for  $\zeta = 0.255$  (thick),  $0.259$  (broken) and  $\bar{Q} = 0.2$  (left),  $0.7$  (right). (The colors blue, brown, green, red, and black, denote the considered quark candidates, Her X-1, SAX J 1808.4-3658, PSR J038-0842, LMC X-4, and SMC X-1, respectively).

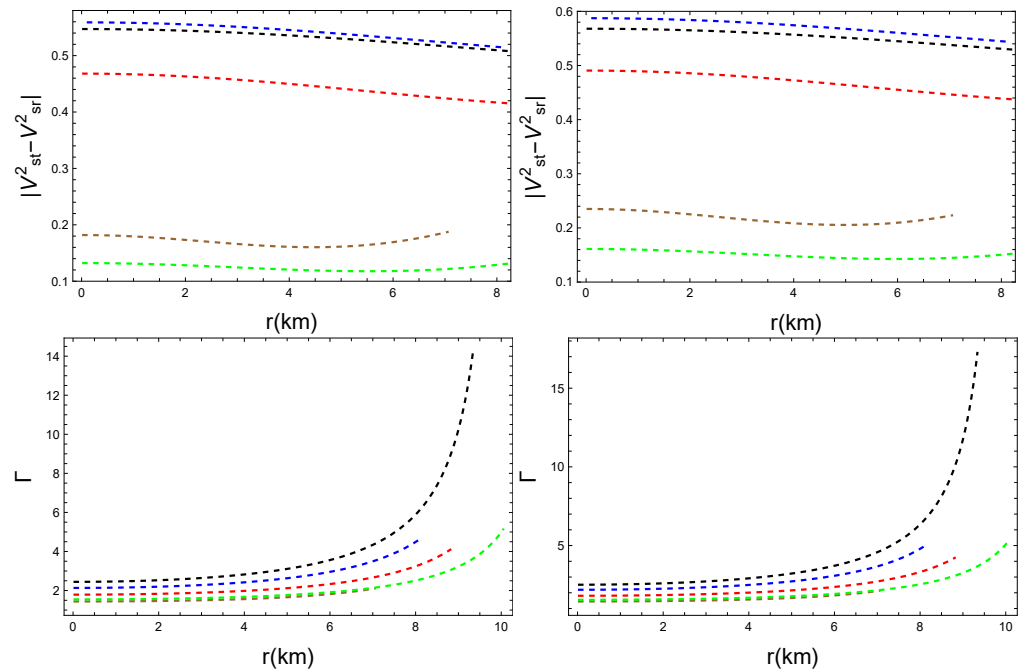


**Figure 16.** Plots of  $|V_{st}^2 - V_{sr}^2|$  and  $\Gamma$  against  $r$  for  $\zeta = 0$  and  $\bar{Q} = 0.2$  (left),  $0.7$  (right). (The colors blue, brown, green, red, and black, denote the considered quark candidates, Her X-1, SAX J 1808.4-3658, PSR J038-0842, LMC X-4, and SMC X-1, respectively).

### 5. Conclusions

In the present work, we have developed a model for strange anisotropic compact stars under electric field within Rastall theory. To examine the structural properties of five different stars, namely, *Her X-1*, *SAX J 1808.4-3658*, *PSR J038-0842*, *LMC X-4*, and *SMC X-1*, we have used MIT bag model EOS together with the field equations of Rastall theory. The Finch–Skea metric potentials that have three constant parameters in the form of  $(A, B, C)$  have been employed, and their values are expressed in terms of star masses and radii using the matching conditions within this theory. A bag constant value of  $\mathcal{B} = 60 \text{ MeV}/\text{fm}^3$  has been chosen for this study. In the analysis of the observational data, the masses and radii of the aforementioned quark star candidates have been used to estimate dimensionless mass–radius ratios, which are discussed in Table 1. In Table 2, these values are further applied to estimate the Finch–Skea parametric values of  $(A, B, C)$ .

To investigate the different physical attributes associated with the quark star candidates, graphical analyses have been performed. We have taken the values of the Rastall and charge parameters to be  $\zeta = 0.255, 0.259$  and  $\bar{Q} = 0.2, 0.7$ , respectively. The thermodynamic variables which comprise  $\bar{\rho}, \bar{P}_r, \bar{P}_t$ , etc., conform to the familiar features of compact stars.

In particular, these quantities are found to be positive and finite, achieving the maximum values at the center. Going outward from the center to the surface, the density and pressures are found to decrease monotonically. Also, a positive anisotropy is noted to be present. The behavior of the energy density is such that there is an inverse relationship with respect to  $\zeta$  and  $\tilde{Q}$ . The redshift and compactness have been found to be within their predicted limits. The energy conditions are completely met, showing that there is normal matter in the inner region of the quark candidates. We mention that while we focus on investigating the impact of the Rastall and charge parameters on various physical properties of the obtained models, no relationship is deduced or established between these parameters, as these parameters are taken as independent variables whose effect on other parameters is investigated in this study.

We have deduced the stability of our model by means of the Herrera cracking technique as well as the adiabatic index, both of which suggest that the stars under consideration remain stable for all parametric values considered. Furthermore, it is noted that the compact star *Her X-1* is found to be more condensed in the perspective of Rastall theory as opposed to  $f(\mathcal{R}, T, \mathcal{Q})$  [35]. On the other hand, *SAX J 1808.4-3658* turns out to be denser in Rastall theory as compared to both  $f(\mathcal{R}, T, \mathcal{Q})$  [35] and  $f(\mathcal{R}, T)$  [56] theories. Three of the stars considered, namely, *Her X-1*, *SAX J 1808.4-3658*, and *SMC X-1*, were also studied in [31] and found to be stable. Finally, our solutions reduce to the solutions of GR in the case where  $\zeta = 0$ .

**Author Contributions:** Formal analysis, Investigation, Software, Writing—original draft. M.S. (Malick Sallah); Conceptualization, Supervision, Validation, Writing—review & editing. M.S. (Muhammad Sharif). All authors have read and agreed to the published version of the manuscript.

**Funding:** This research received no external funding.

**Data Availability Statement:** Data are contained within the article.

**Conflicts of Interest:** The Authors declare no conflict of interest.

## References

1. Psaltis, D. Probes and tests of strong-field gravity with observations in the electromagnetic spectrum. *Living Rev. Relativ.* **2008**, *11*, 9. [[CrossRef](#)] [[PubMed](#)]
2. Will, C.M. The confrontation between general relativity and experiment. *Living Rev. Relativ.* **2014**, *17*, 4. [[CrossRef](#)] [[PubMed](#)]
3. Rastall, P. Generalization of the Einstein theory. *Phys. Rev. D* **1972**, *6*, 3357. [[CrossRef](#)]
4. Rastall, P. A theory of gravity. *Can. J. Phys.* **1976**, *54*, 66. [[CrossRef](#)]
5. Visser, M. Rastall gravity is equivalent to Einstein gravity. *Phys. Lett. B* **2018**, *782*, 83. [[CrossRef](#)]
6. Golovnev, A. More on the fact that Rastall = GR. *Ann. Phys.* **2024**, *461*, 169580. [[CrossRef](#)]
7. Darabi, F.; Moradpour, H.; Licata, I.; Heydarzade, Y.; Corda, C. Einstein and Rastall theories of gravitation in comparison. *Eur. Phys. J. C* **2018**, *78*, 25. [[CrossRef](#)]
8. Singh, A.; Mishra, K.C. Aspects of some Rastall cosmologies. *Eur. Phys. J. Plus* **2020**, *135*, 752. [[CrossRef](#)]
9. Singh, A.; Raushan, R.; Chaubey, R. Qualitative aspects of Rastall gravity with barotropic fluid. *Can. J. Phys.* **2021**, *99*, 1073. [[CrossRef](#)]
10. Singh, A.; Singh, G.P.; Pradhan, A. Cosmic dynamics and qualitative study of Rastall model with spatial curvature. *Int. J. Mod. Phys. A* **2022**, *37*, 2250104. [[CrossRef](#)]
11. Sharif, M.; Sallah, M. Decoupled charged anisotropic spherical solutions in Rastall gravity. *New Astron.* **2024**, *109*, 102198. [[CrossRef](#)]
12. Sharif, M.; Sallah, M. Anisotropic spherical solutions in Rastall gravity by gravitational decoupling. *Eur. Phys. J. Plus* **2024**, *139*, 819. [[CrossRef](#)]
13. Sharif, M.; Sallah, M. Minimally deformed regular Bardeen black hole solutions in Rastall theory. *Chin. J. Phys.* **2024**, *92*, 794. [[CrossRef](#)]
14. Sharif, M.; Sallah, M. Minimally deformed regular Hayward black hole solutions in Rastall theory. *Phys. Scr.* **2024**, *99*, 115031. [[CrossRef](#)]

15. Sharif, M.; Sallah, M. Extended black hole solutions in Rastall theory of gravity. *Astron. Comput.* **2025**, *50*, 100897. [[CrossRef](#)]
16. Einstein, A. The basis of the general theory of relativity. *Ann. Phys.* **1916**, *354*, 769. [[CrossRef](#)]
17. Padilla, A.; Saltas, I.D. A note on classical and quantum unimodular gravity. *Eur. Phys. J. C* **2015**, *75*, 561. [[CrossRef](#)]
18. Hansraj, S.; Banerjee, A. Dynamical behavior of the Tolman metrics in  $f(\mathcal{R}, T)$  gravity. *Phys. Rev. D* **2018**, *97*, 104020. [[CrossRef](#)]
19. Hansraj, S.; Banerjee, A.; Channuie, P. Impact of the Rastall parameter on perfect fluid spheres. *Ann. Phys.* **2019**, *400*, 320. [[CrossRef](#)]
20. Witten, E. Cosmic separation of phases. *Phys. Rev. D* **1984**, *30*, 272. [[CrossRef](#)]
21. Dey, M.; Bombaci, I.; Dey, J.; Ray, S.; Samanta, B.C. Strange stars with realistic quark vector interaction and phenomenological density-dependent scalar potential. *Phys. Lett. B* **1998**, *438*, 123. [[CrossRef](#)]
22. Herrera, L. Cracking of self-gravitating compact objects. *Phys. Lett. A* **1992**, *165*, 206. [[CrossRef](#)]
23. Kalam, M.; Rahaman, F.; Molla, S.; Hossein, S.M. Anisotropic quintessence stars. *Astrophys. Space Sci.* **2014**, *349*, 865. [[CrossRef](#)]
24. Paul, B.C.; Deb, R. Relativistic solutions of anisotropic compact objects. *Astrophys. Space Sci.* **2014**, *354*, 421. [[CrossRef](#)]
25. Tangphati, T.; Banerjee, A.; Hansraj, S.; Pradhan, A. The criteria of the anisotropic quark star models in Rastall gravity. *Ann. Phys.* **2023**, *452*, 169285. [[CrossRef](#)]
26. Salako, I.G.; Boko, R.; Baffou, E.; Arouko, M.Z. Anisotropic quintessence charged strange stars in Rastall-Maxwell gravity. *Mod. Phys. Lett. A* **2022**, *37*, 2250053. [[CrossRef](#)]
27. Panotopoulos, G.; Rincón, Á. Relativistic strange quark stars in Lovelock gravity. *Eur. Phys. J. Plus* **2019**, *134*, 472. [[CrossRef](#)]
28. Lopes, I.; Panotopoulos, G.; Rincón, Á. Anisotropic strange quark stars with a non-linear equation-of-state. *Eur. Phys. J. Plus* **2019**, *134*, 454. [[CrossRef](#)]
29. Bhar, P. Strange star with Krori-Barua potential in the presence of anisotropy. *Int. J. Geom. Methods Mod. Phys.* **2021**, *18*, 2150097. [[CrossRef](#)]
30. Shahzad, M.R.; Abbas, G. Strange stars with MIT bag model in the Rastall theory of gravity. *Int. J. Geom. Methods Mod. Phys.* **2019**, *16*, 1950132. [[CrossRef](#)]
31. Mustafa, G.; Errehymy, A.; Ditta, A.; Daoud, M. Charged strange stars with dust and phantom regimes in Rastall gravity. *Chin. J. Phys.* **2022**, *77*, 2781. [[CrossRef](#)]
32. Banerjee, A.; Tangphati, T.; Hansraj, S.; Pradhan, A. Strange quark star models from Rastall gravity. *Ann. Phys.* **2023**, *451*, 169267. [[CrossRef](#)]
33. Sharif, M.; Naseer, T. Study of Charged Compact Stars in Non-minimally Coupled Gravity. *Fortschr. Phys.* **2023**, *71*, 2200147. [[CrossRef](#)]
34. Sharif, M.; Naseer, T. Anisotropic stellar models with Tolman IV space-time in non-minimally coupled theory. *Pramana J. Phys.* **2024**, *98*, 25. [[CrossRef](#)]
35. Sharif, M.; Naseer, T. Estimating the role of bag constant and modified theory on anisotropic stellar models. *Chin. J. Phys.* **2024**, *88*, 10.
36. Bordbar, G.H.; Peivand, A.R. Computation of the structure of a magnetized strange quark star. *Res. Astron. Astrophys.* **2011**, *11*, 851. [[CrossRef](#)]
37. Haensel, P.; Zdunik, J.L.; Schaefer, R. Strange quark stars. *Astron. Astrophys.* **1986**, *160*, 121.
38. Mak, M.K.; Harko, T. An exact anisotropic quark star model. *Chin. J. Astrophys.* **2002**, *2*, 248. [[CrossRef](#)]
39. Rahaman, F.; Chakraborty, K.; Kuhfittig, P.K.F.; Shit, G.C.; Rahman, M. A new deterministic model of strange stars. *Eur. Phys. J. C* **2014**, *74*, 3126. [[CrossRef](#)]
40. Bhar, P. A new hybrid star model in Krori-Barua spacetime. *Astrophys. Space Sci.* **2015**, *357*, 1. [[CrossRef](#)]
41. Arbañil, J.D.V.; Malheiro, M. Stability of charged strange quark stars. *AIP Conf. Proc.* **2015**, *1693*, 030007.
42. Deb, D.; Chowdhury, S.R.; Ray, S.; Rahaman, F.; Guha, B.K. Relativistic model for anisotropic strange stars. *Ann. Phys.* **2017**, *387*, 239. [[CrossRef](#)]
43. Deb, D.; Khlopov, M.; Rahaman, F.; Ray, S.; Guha, B.K. Anisotropic strange stars in the Einstein-Maxwell spacetime. *Eur. Phys. J. C* **2018**, *78*, 465. [[CrossRef](#)]
44. Sharif, M.; Waseem, A. Anisotropic quark stars in  $f(\mathcal{R}, T)$  gravity. *Eur. Phys. J. C* **2018**, *78*, 868. [[CrossRef](#)]
45. Majid, A.; Sharif, M. Quark stars in massive Brans-Dicke gravity with Tolman-Kuchowicz spacetime. *Universe* **2020**, *6*, 124. [[CrossRef](#)]
46. Fiorella Burgio, G.; Fantina, A.F. Nuclear equation of state for compact stars and supernovae. *Astrophys. Space Sci. Libr.* **2018**, *457*, 255.
47. Finch, M.R.; Skea, J.E.F. A realistic stellar model based on an ansatz of Duorah and Ray. *Class. Quantum Gravity* **1989**, *6*, 467. [[CrossRef](#)]
48. Abubekkerov, M.K.; Antokhina, E.A.; Cherepashchuk, A.M.; Shimanskii, V.V. The mass of the compact object in the X-ray binary her X-1/Hz her. *Astron. Rep.* **2008**, *52*, 379. [[CrossRef](#)]

49. Li, X.D.; Bombaci, I.; Dey, M.; Dey, J.; Van Den Heuvel, E.P.J. Is SAX J1808.4-3658 a strange star? *Phys. Rev. Lett.* **1999**, *83*, 3776. [[CrossRef](#)]
50. Rawls, M.L.; Orosz, J.A.; McClintock, J.E.; Torres, M. A.; Bailyn, C.D.; Buxton, M.M. Refined neutron star mass determinations for six eclipsing x-ray pulsar binaries. *Astrophys. J.* **2011**, *730*, 25. [[CrossRef](#)]
51. Buchdahl, H.A. General relativistic fluid spheres. *Phys. Rev.* **1959**, *116*, 1027. [[CrossRef](#)]
52. Li, R.; Wang, J.; Xu, Z.; Guo, X. Constraining the Rastall parameters in static space-times with galaxy-scale strong gravitational lensing. *Mon. Not. R. Astron. Soc.* **2019**, *486*, 2407. [[CrossRef](#)]
53. Ivanov, B.V. Static charged perfect fluid spheres in general relativity. *Phys. Rev. D* **2002**, *65*, 104011. [[CrossRef](#)]
54. Abreu, H.; Hernandez, H.; Nunez, L.A. Sound speeds, cracking and the stability of self-gravitating anisotropic compact objects. *Class. Quantum Grav.* **2007**, *24*, 4631. [[CrossRef](#)]
55. Heintzmann, H.; Hillebrandt, W. Neutron stars with an anisotropic equation of state-mass, redshift and stability. *Astron. Astrophys.* **1975**, *38*, 51.
56. Rej, P.; Bhar, P.; Govender, M. Charged compact star in  $f(\mathcal{R}, T)$  gravity in Tolman-Kuchowicz spacetime. *Eur. Phys. J. C* **2021**, *81*, 316. [[CrossRef](#)]

**Disclaimer/Publisher's Note:** The statements, opinions and data contained in all publications are solely those of the individual author(s) and contributor(s) and not of MDPI and/or the editor(s). MDPI and/or the editor(s) disclaim responsibility for any injury to people or property resulting from any ideas, methods, instructions or products referred to in the content.